THE JOURNAL OF PHYSICAL CHEMISTRY LETTERS
A JOURNAL OF THE AMERICAN CHEMICAL SOCIETY

pubs.acs.org/JPCL
Letter

Operando Nanomechanical Mapping of Amorphous Silicon Thin Film Electrodes in All-Solid-State Lithium-Ion Battery Configuration during Electrochemical Lithiation and Delithiation

Ridwan P. Putra, Kyosuke Matsushita, Tsuyoshi Ohnishi, and Takuya Masuda*

Cite This: *J. Phys. Chem. Lett.* 2024, 15, 490−498

Read Online

ACCESS | Metrics & More | Article Recommendations | Supporting Information

ABSTRACT: An *operando* bimodal atomic force microscopy system was constructed to perform nanomechanical mapping of an amorphous Si thin film electrode deposited on a $Li_{6.6}La_3Zr_{1.6}Ta_{0.4}O_{12}$ solid electrolyte sheet during electrochemical lithiation/delithiation. The evolution of Young's modulus maps of the Si electrode was successfully tracked as a function of apparent Li content x in lithium silicide (Li_xSi) simultaneously with real-time surface topography observation. At the initial stage of lithiation, the average modulus steeply decreased due to the generation of Li_xSi from intrinsic Si, followed by a moderate modulus reduction until the electrode capacity reached 3300 mAh g^{-1} (Li content x = 3.46). In the following delithiation, the gradual recovery of the average modulus of Li_xSi was observed up to 1467 mAh g^{-1} (Li content x = 1.54) at which delithiation stopped due to the significant volume change induced by phase transformation of Li_xSi.

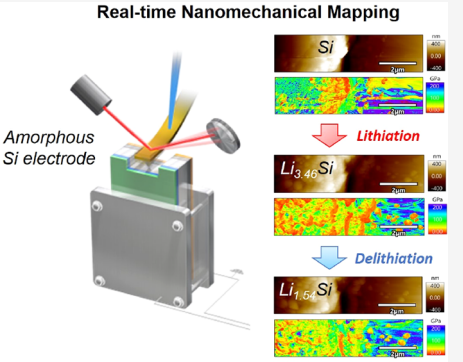

Li-ion batteries (LIBs) are the most mature energy storage technologies in electric vehicles and portable electronic devices due to their high energy densities and low self-discharge rates.[1−3] Unfortunately, conventional LIBs still suffer from safety issues because of the employment of flammable liquid organic electrolytes.[4] In this regard, research efforts have been devoted to the development of all-solid-state Li-ion batteries (ASSLIBs), which demonstrate relatively high chemical safety, low flammability, and wide electrochemical potential windows due to the substitution of liquid organic electrolytes with solid-state electrolytes.[5−7]

Toward the high-performance next-generation batteries, silicon is considered one of the most promising candidates as an anode material for both conventional liquid-type LIBs[8−11] and ASSLIBs,[12,13] due to its extremely high theoretical specific capacity density at room temperature (3579 mAh g^{-1}) and low lithiation/delithiation potential (~0.4 V vs Li^+/Li).[14−18] Nevertheless, Si undergoes severe volume expansion/contraction during electrochemical lithiation/delithiation, resulting in poor cycle and rate performance of the electrode.[12,19] These phenomena are caused by the changes in the lattice structure as well as phase transitions in Si upon the insertion/release of Li ions, leading to cracking, pulverization, and fracture of the particles and/or electrodes.[20,21] For these reasons, several fabrication techniques to produce Si anodes with improved electrode performance and cycle life have been developed, including the slurry-based synthesis approach,[13] spray deposition,[12] electrophoretic deposition,[22] electron-beam evaporation,[23] pulsed-laser deposition,[24] and magnetron sputtering.[25]

Recently, an *operando* X-ray photoelectron spectroscopy (XPS) study on amorphous Si thin film electrodes revealed the formation of amorphous lithium silicide Li_xSi ($0 < x < 3.5$) and a metastable crystalline $Li_{15}Si_4$ phase throughout the first lithiation up to x = 3.5, followed by the phase transition of crystalline $Li_{15}Si_4$ to the amorphous phase in the successive delithiation.[26] The reversible capacity of lithiation/delithiation cycles up to the formation of $Li_{3.5}Si$ where the phase transition occurs, was more rapidly decayed than that of $Li_{2.4}Si$ where the phase transition does not occur. Thus, the local mechanical stress caused by the phase transition from crystalline $Li_{15}Si_4$ to amorphous Li_xSi is considered a primary factor of relatively rapid capacity fading. The nanomechanical properties of Li_xSi species depends on the Li content x which is changed by the lithiation/delithiation.[21] Further, the heterogeneity in the mesoscale distribution of Li_xSi can induce local mechanical stresses within the particles and/or electrodes, especially when the two-phase regions are involved.[16,27,28] Those multiscale physicochemical events significantly affect the bulk mechanical properties of the electrode and macroscale cell performance, as predicted by numerical simulations and machine learning studies.[29] Therefore, it is very important to clarify and manage

Received: October 27, 2023
Revised: December 30, 2023
Accepted: January 3, 2024

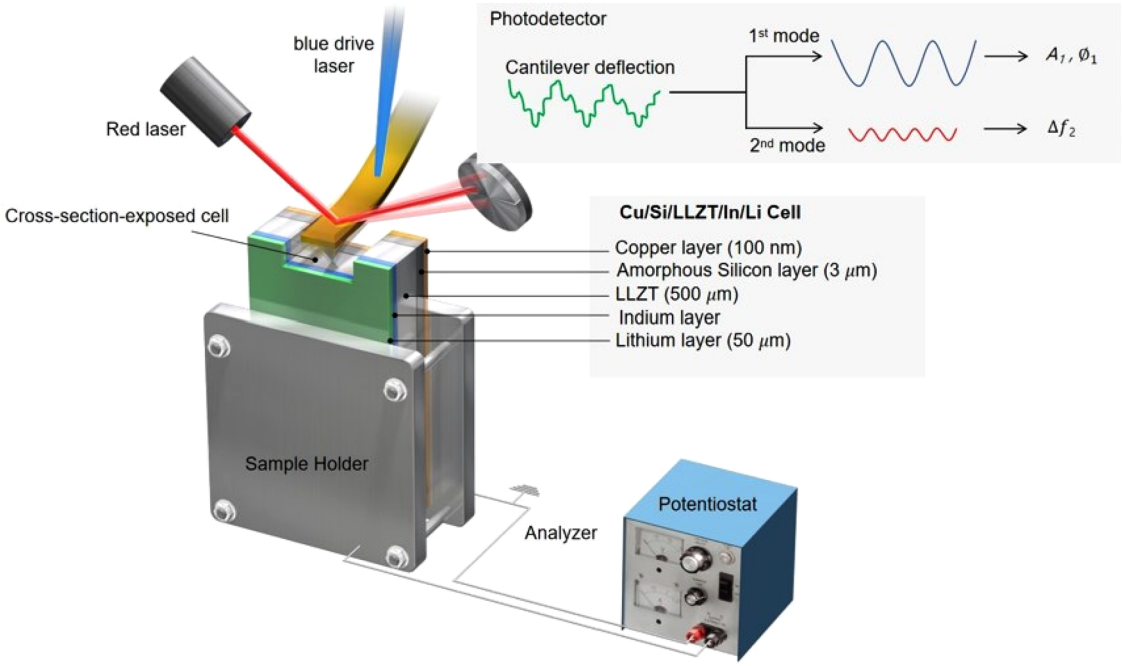

Figure 1. Schematic illustration of the cross-section-exposed Cu/Si/LLZT/In/Li cell mounted on a custom-made sample holder coupled with a potentiostat for *operando* nanomechanical mapping on bimodal AFM.

such nanomechanical events in order to mitigate mechanical degradation and the failure of the electrodes.

To date, several studies have been carried out to quantify the mechanical properties of Li_xSi. Theoretical studies on the bulk moduli of amorphous and crystalline Li_xSi by the first-principles calculations show elastic modulus reduction/gain with increasing/decreasing Li content x in Li_xSi.[21,28] The decrease in the bulk modulus of Li_xSi with increasing Li content x is attributed to the structural transformation upon Li-ion insertion.[21]

Zeng et al. (2013) experimentally measured the bulk modulus of a metastable polycrystalline $Li_{15}Si_4$ phase using *in situ* high-pressure synchrotron X-ray diffraction (XRD) at room temperature. The modulus obtained from their study follows a linear relationship with the modulus of pure Li and Si.[30] Meanwhile, the bulk moduli of crystalline $Li_{12}Si_7$ and Li_7Si_3 evaluated using the same technique exhibit a nonlinear behavior with respect to the ratio of Li to Si.[31] Using an *ex-situ* nanoindentation technique, Hertzberg et al. (2011) studied the Young's moduli of $Li_{0.6}Si$, $Li_{1.08}Si$, $Li_{2.06}Si$, and $Li_{3.75}Si$ upon the first lithiation of a nanocrystalline Si electrode film. The measured moduli are in line with a linear rule of mixtures up to a Li fraction of 0.375, while a constant modulus is attained when the Li fraction is within the range 0.52−0.67.[32] Nonetheless, using the currently available techniques, it is difficult to elucidate the changes in the mechanical properties of various Li_xSi species under electrochemical lithiation and delithiation, which are essential in the design and fabrication of highly durable electrodes. Thus, only a few experimental studies on the mechanical properties of various Li_xSi species have been reported, possibly due to the challenges of experimental techniques and difficulties in obtaining stable Li_xSi phases under ambient conditions.

Atomic force microscopy (AFM) is a powerful tool for revealing real-time morphological evolution and physicochemical properties of a wide variety of solid surfaces[33−38] including battery materials.[39−44] Recent breakthroughs, known as the bimodal AFM, enables a nondestructive nanomechanical property mapping for a wide range of Young's modulus (1 MPa−200 GPa) simultaneously with surface topography imaging at a high-speed and high-spatial resolution by detecting the changes of amplitude and frequency of excited first and higher eigen-mode resonant vibrations of cantilever.[45,46] Previously, our group applied this technique to perform nanomechanical mapping of composite $LiCoO_2$ and graphite electrodes composed of active materials, binders, and conductive agents. The nanoscale moduli of the electrode materials in the pristine and fully charged states were successfully distinguished and quantified from the acquired Young's modulus maps.[44] Using the same method, Yang et al. (2021) investigated the topographic and nanomechanical evolutions of $LiMn_2O_4$ cathode films upon several charge/discharge cycles to study the degradation mechanisms of the materials.[47] In these studies, the *ex-situ* characterizations were performed after several electrochemical treatments and disassembly of the cells, which may lead to misinterpretation of the actual phenomena taking place in the electrodes due to the sample inhomogeneity under different probed areas and voltage relaxation during sample transfer to the measurement apparatuses.[48,49]

Therefore, here we developed an *operando* bimodal AFM system to carry out nanomechanical mapping of an amorphous Si thin film electrode in an all-solid-state battery configuration during the first electrochemical lithiation and delithiation. The Young's modulus was selected to represent the nanomechanical property of the electrode because it indicates how strain develops in the electrode when a certain amount of force is applied.[44,50] The changes in the Young's modulus maps of the Si electrode were successfully observed simultaneously with topography images in real-time, and the average Young's moduli of the Si electrode at different Li contents x in Li_xSi were quantitatively determined.

https://doi.org/10.1021/acs.jpclett.3c03012
J. Phys. Chem. Lett. 2024, 15, 490−498

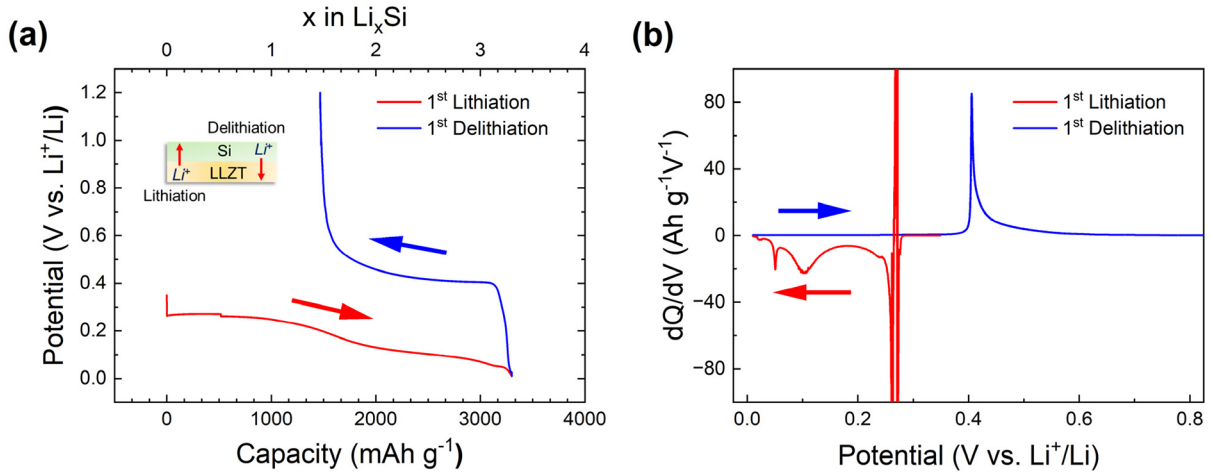

Figure 2. (a) Galvanostatic profiles and (b) generated dQ/dV curves during the first lithiation/delithiation of the Si thin film electrode in the Cu/Si/LLZT/In/Li cell.

A Cu/Si/$Li_{6.6}La_3Zr_{1.6}Ta_{0.4}O_{12}$ (LLZT)/In/Li cell was prepared following the protocol described earlier with a few modifications.[26,51] Initially, one side of a 500 μm thick garnet-type LLZT solid electrolyte sheet (Toshima Manufacturing Co., Ltd.) was sandblasted with 220 grit alumina powder to obtain a rough surface. After annealing at 700 °C for 2 h, the LLZT was immersed in an aqueous solution saturated with LiOH for 1 h to remove the resistive species, e.g., LiOH and Li_2CO_3.[14] Amorphous Si thin film with a thickness of 3 μm was deposited on the sandblasted side of the LLZT solid electrolyte sheet by radio frequency magnetron sputtering under Ar atmosphere. Cu layer with a thickness of 100 nm was subsequently deposited on the Si thin film by direct current sputtering and used as the current collector. Afterward, a thin In layer (5 nm) was sputter-deposited on the other side of the LLZT electrolyte to yield a sample with a structure of Cu/Si/LLZT/In. Prior to combining the Cu/Si/LLZT/In sample with 50 μm thick Li metal (Honjo Metal Co., Ltd.), the cross-section of the sample was polished using an Ar-ion beam to obtain the flat and smooth Cu/Si/LLZT/In cross-section required for AFM analysis.

The cross-section polishing of the Cu/Si/LLZT/In sample was performed on a Hitachi ArBlade-5000 at accelerating and discharge voltages of 8.0 and 2.0 kV, respectively, for 3 h. The sample was initially placed on the sample holder, with a Ti mask facing the Cu side of the Cu/Si/LLZT/In sample; thus, the Cu layer was the first layer milled by the Ar-ion beam. The Ti mask was cooled to −100 °C using liquid nitrogen throughout the milling process. The cross-section-exposed Cu/Si/LLZT/In sample was subsequently combined with Li metal to yield a cell with a configuration of Cu/Si/LLZT/In/Li. Here, the Si film and Li metal worked as the working and counter electrodes, respectively. Prevention of damage to cells during ion milling is one of the challenges in the present work. A few typical failures are shown in the Supporting Information.

The cross-section-exposed Cu/Si/LLZT/In/Li cell was mounted on a custom-made sample holder made of stainless-steel before being inserted into the bimodal AFM instrument (Cypher ES, Asylum Research, Oxford Instruments), as illustrated in Figure 1. Appropriate confining pressure was applied by a metal screw when sandwiching the Cu/Si/LLZT/In/Li cell between the stainless-steel plates. The sample holder was connected to a potentiostat (SP-50, BioLogic Science Instruments) for the bias applications during lithiation/deltihation. All the experiments were conducted inside an Ar-filled glovebox (O_2 < 0.1 ppm, H_2O < 0.1 ppm) to avoid any oxygen and moisture contaminations.

The *operando* nanomechanical mapping was performed during the first lithiation and delithiation of the Si thin film electrode within a potential window of 0.01−1.20 V. The potentials reported in this study were measured against the Li^+/Li reference.

The galvanostatic potential profiles of the Cu/Si/LLZT/In/Li cell in the first lithiation/delithiation carried out within a potential window of 0.01−1.20 V are shown in Figure 2a. The first lithiation was started at a low constant current density of 14.59 μA cm^{-2} (0.005 C) for 25 h from the open circuit potential (OCP, 0.35 V), followed by the application of a higher constant current density of 29.19 μA cm^{-2} (0.010 C) until 0.01 V. Subsequently, the successive delithiation was performed at a constant current density of 29.19 μA cm^{-2} (0.010 C) up to 1.20 V. The upper axis indicates the apparent Li content x in Li_xSi, estimated from the integrated electrical charge at the bottom axis during lithiation/delithiation and the number of Si atoms present in the thin film electrode. The first lithiation capacity density of the Si electrode was 3300 mAh g^{-1} (Li content x = 3.46), which is close to the theoretical capacity at room temperature (3579 mAh g^{-1}) of a Si electrode.[16,52] In addition to the measured capacity density, the shape of galvanostatic profile during the first lithiation is comparable to our previous study employing Si/LLZT/Li cell with a thinner amorphous Si film of ca. 95.0 nm, despite increased film thickness.[26,51]

Although the first lithiation capacity of the Si electrode reached 3300 mAh g^{-1}, the successive delithiation capacity observed in this study was only 1833 mAh g^{-1} (=3300−1467 mAh g^{-1}, Li content x = 1.54). The cause of the low delithiation capacity is the incompletion of delithiation, most likely due to the decrease in confining pressure of the cell sandwiched by the sample holder, which was induced by a significant volume change during the delithiation. Thus, the delithiation in this study stopped at a potential of ∼0.41 V where the phase transformation of crystalline Li_xSi to amorphous takes place, as discussed in the following section.

Figure 2b shows the negative and positive dQ/dV curves of the thin film electrode during the first lithiation and

https://doi.org/10.1021/acs.jpclett.3c03012
J. Phys. Chem. Lett. 2024, 15, 490−498

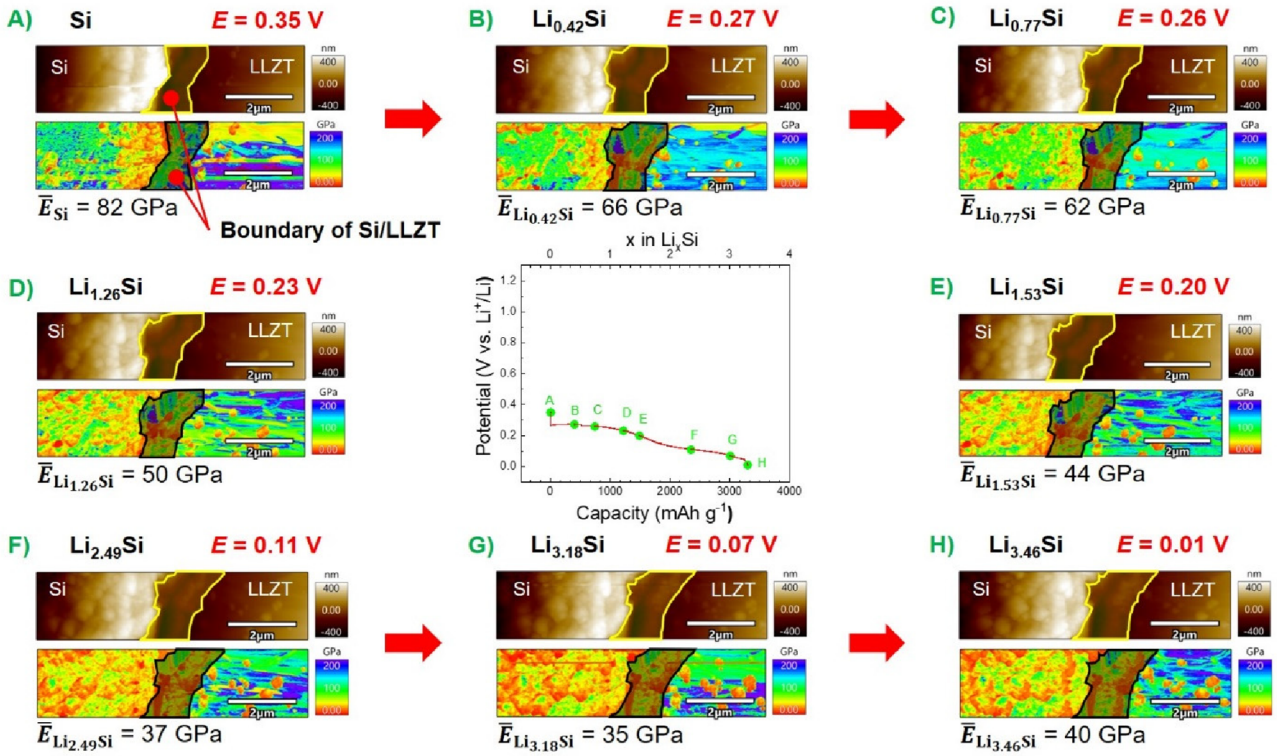

Figure 3. Topography images and Young's modulus maps of the Si thin film electrode in the Cu/Si/LLZT/In/Li cell during the first lithiation. The masked areas indicate the boundaries of the Si/LLZT.

delithiation, respectively, obtained from the differentiation of the smoothed galvanostatic profiles in Figure 2a. Two sharp peaks observed at 0.27 and 0.26 V in the negative dQ/dV curve are attributed to the two-step lithiation process of amorphous Si electrode to amorphous Li_xSi.[11,53] A positive dQ/dV peak was detected at 0.27 V in the negative dQ/dV curve, probably due to the transition from lower to higher current densities in the first lithiation. Further lithiation of the Li-poor to -rich amorphous Li_xSi phase was characterized by a broad peak observed at 0.10 V.[53] At a potential of 0.05 V, a small peak corresponding to the transformation of amorphous Li_xSi to crystalline $Li_{3.75}Si$ was detected.[16,53] The presence of an overlithiated crystalline phase, $Li_{3.75+\delta}$ (δ = 0.2−0.3), was also observed, as indicated by a shoulder at 0.02 V in the negative dQ/dV curve.[54]

The positive dQ/dV curve shows a single sharp peak at 0.41 V, which corresponds to the phase transition of crystalline $Li_{15}Si_4$ to amorphous Li_xSi.[53,55] The generation of crystalline $Li_{15}Si_4$ phase in the first lithiation, followed by the phase transformation of the $Li_{15}Si_4$ to amorphous Li_xSi in the subsequent delithiation, may induce a significant volume change and decrease in confining pressure within the thin film cell, resulting in the incompletion of delithiation at this stage.

The topography imaging and nanomechanical mapping were performed on the cross section around the Si/LLZT interface using a Si cantilever (AC160TSA) with spring constants of 23.93 and 772.2 nN/nm for the first and second eigenmodes, respectively. The LLZT was used as an internal standard to calibrate the acquired Young's modulus maps, as the contact radius of the tip and sample (R) tends to change throughout the scanning, which can affect the measured Young's modulus values.[45] The measurement was conducted over a scan size of 8 μm × 2 μm at a scan rate of 0.1 Hz. The amplitude modulation-frequency modulation (AM-FM) mode of the bimodal AFM was employed to acquire Young's modulus maps simultaneously with the topography images, and the effective Young's modulus (E_{eff}) was extracted using the Hertz contact model with a flat punch, as justified in eq 1, where R indicates the contact radius of the tip and sample, k_1, Q_1, $A_{1,free}$, $A_{1,set}$, and θ_1 are the spring constant, quality factor, free oscillation amplitude, set point amplitude, and phase of the first eigenmode of the cantilever, while k_2, Δf_2, and f_2 are the spring constant, frequency shift, and frequency of the second eigenmode of the cantilever.[45,56] Prescanning treatment was performed on a "dummy" scan area for 12 h before the main experiment in order to stabilize the tip−sample contact radius.

$$E_{eff} = \frac{\pi}{R}\sqrt{\frac{1}{6}}\left(\frac{k_1}{Q_1}\frac{A_{1,free}}{A_{1,set}}\cos\theta_1\right)^{-1/2}\left(\frac{2k_2\Delta f_2}{f_2}\right)^{3/2} \quad (1)$$

Young's modulus of the sample (E_s) was determined using eq 2, where ν_t is Poisson's ratio of the tip, E_t is Young's modulus of the tip, and ν_s is Poisson's ratio of the sample.[45,56]

$$\frac{1}{E_{eff}} = \frac{1-\nu_t^2}{E_t} + \frac{1-\nu_s^2}{E_s} \quad (2)$$

Here, Young's modulus of the tip was assumed to be 150 GPa, while Poisson's ratios of the tip and sample were assumed to be 0.17 and 0.26, respectively.[44,57−59] The images presented in this work were processed and analyzed using modified Igor Pro 6.38B01 with Asylum Research 16.26.229 add-on and/or ImageJ software.[60]

As mentioned above, the Young's modulus maps were calibrated using the bulk modulus of LLZT as the internal standard.[45] The calibration was carried out using modified Igor

https://doi.org/10.1021/acs.jpclett.3c03012
J. Phys. Chem. Lett. 2024, 15, 490−498

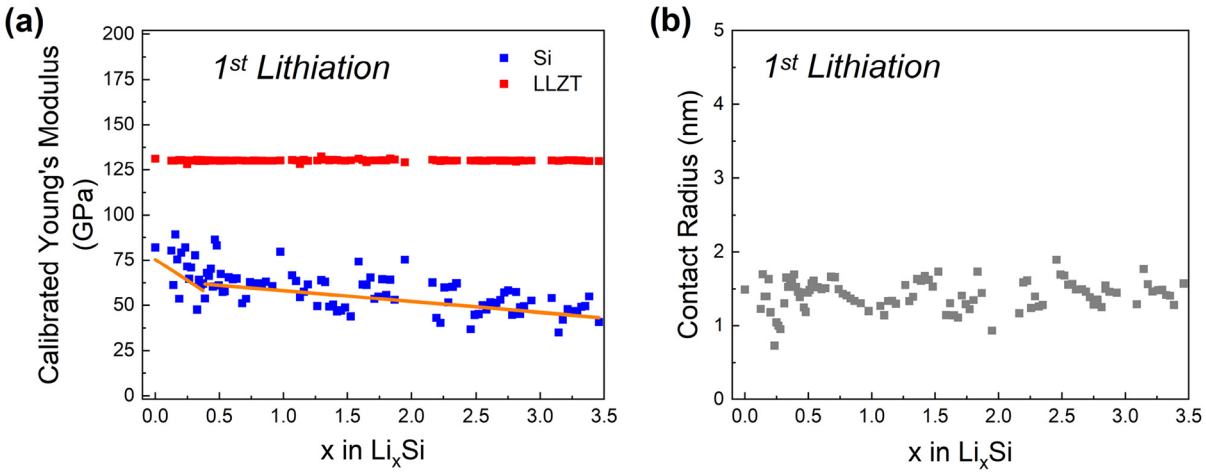

Figure 4. (a) Average Young's moduli of the Si thin film electrode after calibration using LLZT as an internal standard and (b) contact radius of the tip and sample during the first lithiation of the Si thin film electrode in the Cu/Si/LLZT/In/Li cell with outliers (|SR| > 2.5) excluded.

Pro 6.38B01 with Asylum Research 16.26.229 add-on, employing the Hertz contact model with a flat punch tip, as eqs 1 and 2.[45,56] The bulk modulus of LLZT was initially measured on a nanoindenter (iNano Nanoindenter, KLA-Tencor) using a Berkovich pyramidal diamond tip, and Oliver and Phar method was used to extract the bulk modulus from the recorded load−displacement curves.[61] From the measurements, it was found that the bulk modulus of LLZT was in the range 100−150 GPa, which is consistent with the values from the literature.[62] Here, a Young's modulus value of 130 GPa was selected as the modulus of LLZT to perform the calibration on the acquired Young's modulus maps. We assumed that there is no significant change in the Young's modulus of LLZT throughout the first lithiation and delithiation of the Si electrode.

Figure 3 shows the topography images and Young's modulus maps simultaneously recorded throughout the first lithiation from x = 0 up to x = 3.46 in Li_xSi. The topography images show the roughening of the Si surface with increasing Li content x in Li_xSi, due to the expansion accompanying with lithiation. The average size of the Si particles was found to increase from 167 nm in Si to 446 nm in $Li_{3.46}Si$. Meanwhile, the shift of the Si/LLZT interface toward the Li counter electrode was also observed, most likely due to the expansion of the Si electrode film and/or the contraction of the Li electrode during the first lithiation.[63,64]

Calibrated Young's modulus maps of the Si thin film electrode suggest spatially nonuniform Young's modulus reduction with increasing Li content x in Li_xSi. In general, the areas with low Young's modulus values, indicated by the red color, tended to increase as more Li was inserted into the Si thin film. The nonuniform distribution of Young's modulus at each measurement point can be attributed to the variation of thermal drifting of the tip and contact area between the tip and surface during the AFM measurements, as well as the inhomogeneous reaction distribution due to the use of sputter-deposited amorphous Si.

Some spherical particles with relatively low modulus values were observed on the surface of the LLZT solid electrolyte. These particles may be the Li_xSi particles exfoliated from the electrode that are dragged and dropped by the AFM tip throughout the measurement. Occasionally, some areas in the Young's modulus maps were not successfully acquired. Hence, the calibration of the Young's modulus maps was carried out by omitting the soft particles present on the surface of LLZT, which was used as the internal standard,[45] in addition to the unsuccessfully mapped areas and Si/LLZT boundaries. The average Young's modulus of the Si electrode at different Li content x was calculated from the average measured modulus of the Si surface at the cross-section.

The average Young's moduli of the Si thin film electrode throughout the first lithiation were plotted as a function of Li content x in Li_xSi to estimate the trend of elastic modulus change with increasing x, as shown in Figure S4. As the modulus of the Si electrode generally decreases with increasing x, we assume that there are some potential outliers. Therefore, standardized residual (SR) analysis was performed to identify the outliers,[65,66] and the measured moduli with |SR| > 3, 2.5, and 2 were excluded from the data set. The average moduli of the Si thin film electrode throughout the first lithiation with outliers (|SR| > 2.5) excluded are presented in Figure 4a. The average modulus of pristine Si measured in the present work is within the range of acceptable modulus of pure Si reported in the literature,[21,28,67−69] confirming the reliability of Young's modulus measured by this technique. In the initial stage of lithiation, in the range of Li content x = 0−0.37, the modulus steeply decreased due to the formation of Li_xSi from pristine Si, followed by a moderate modulus reduction with a further increase in Li content x. A similar phenomenon was observed in our previous *operando* XPS study in the first electrochemical lithiation of amorphous Si electrode; the peak position corresponding to pristine bulk Si 2p shifted to lower binding energy steeply in the range of Li content x = 0−0.13, and then moderately.[26] Those initial drastic changes of Young's modulus and Si 2p photoelectron peak position are attributable to the difference in electronic structures of pure Si and Li_xSi.[21,70]

The changes in the contact radius R of the tip and sample during the first lithiation are presented in Figure 4b. The R varied from 0.73 to 1.89 nm, which were within the range to perform nanomechanical mapping by the bimodal AFM (within a few nanometer).[45] The moduli of various Li_xSi species from this study are also consistent with those obtained from theoretical calculations.[21,28]

The topography images and calibrated Young's modulus maps of the Si electrode in the successive delithiation are shown in Figure 5. The nanomechanical mapping was

https://doi.org/10.1021/acs.jpclett.3c03012
J. Phys. Chem. Lett. 2024, 15, 490−498

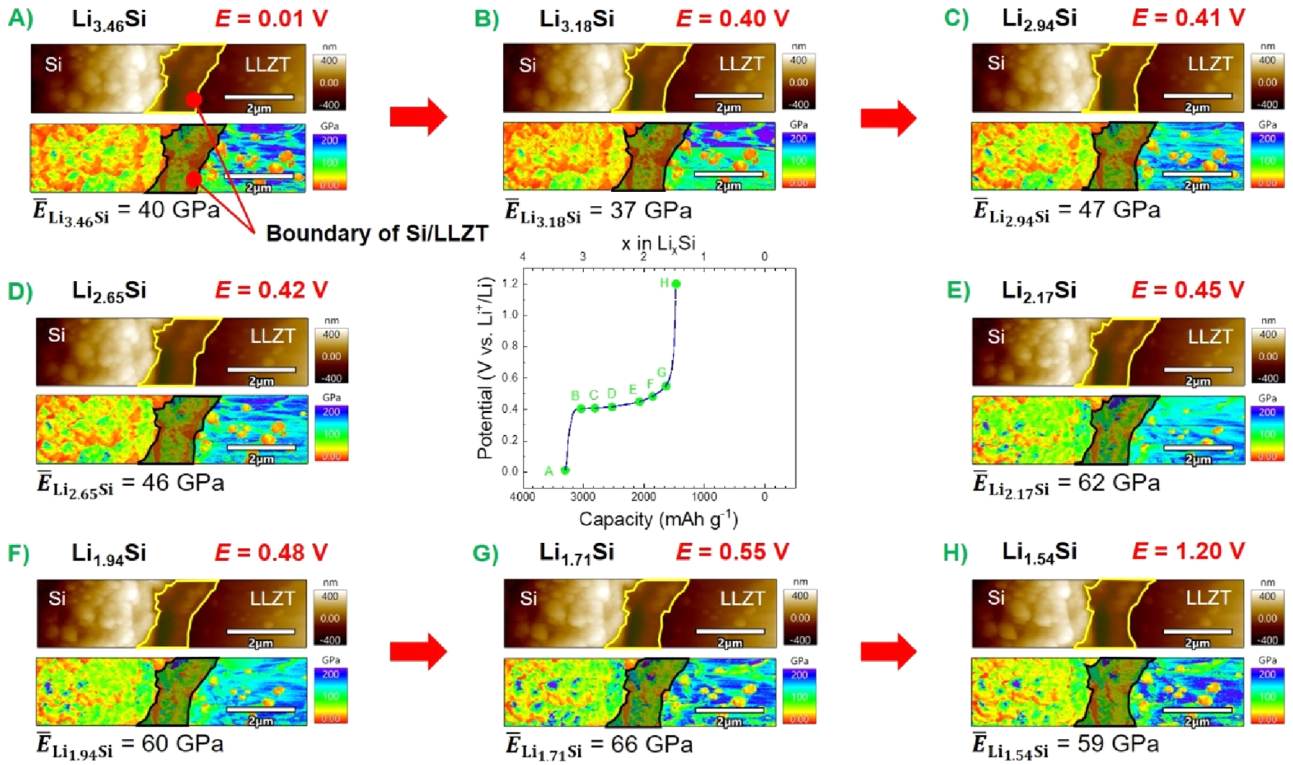

Figure 5. Topography images and Young's modulus maps of the Si thin film electrode in the Cu/Si/LLZT/In/Li cell during the first delithiation. The masked areas indicate the boundaries of the Si/LLZT.

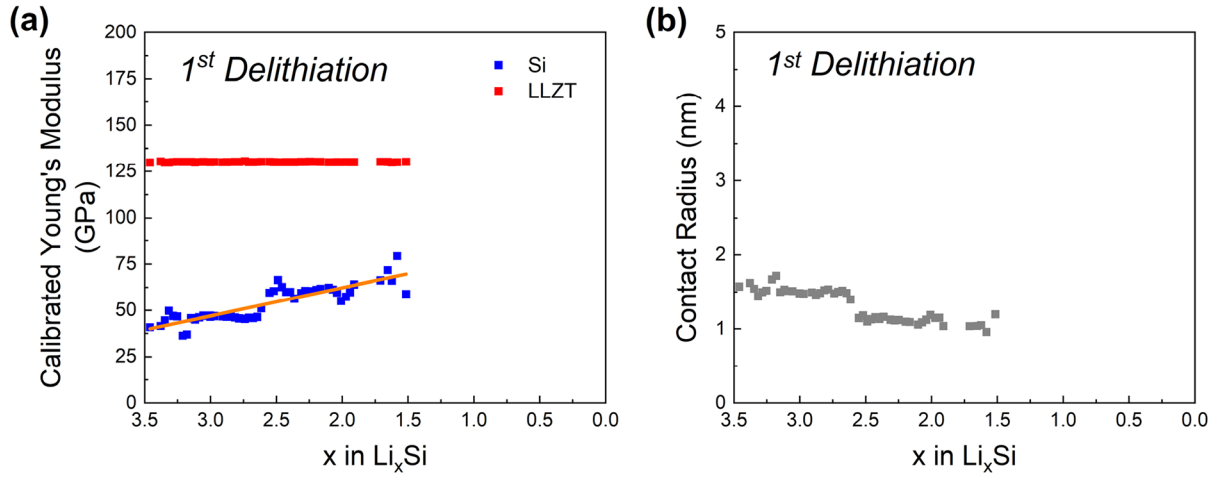

Figure 6. (a) Average Young's moduli of the Si thin film electrode after calibration using LLZT as an internal standard and (b) contact radius of the tip and sample during the first delithiation of the Si thin film electrode in the Cu/Si/LLZT/In/Li cell with outliers (|SR| > 2.5) excluded.

conducted only up to Li content x = 1.54 in Li_xSi because the delithiation stopped at this level possibly due to the mechanical failure induced by phase transformation of crystalline $Li_{15}Si_4$ to amorphous Li_xSi.[26] No significant changes were observed in the topography of the Si electrode. Calibrated Young's modulus maps of the Si electrode during the first delithiation showed gradual recovery of the elastic modulus in the areas at which the lithiation took place during the first lithiation. In general, the average modulus of Li_xSi increases with decreasing Li content x in Li_xSi during delithiation, although the fluctuation in the recorded values were observed (Figure 5). This is probably due to the coexistence of crystalline $Li_{15}Si_4$ and amorphous Li_xSi[26] and/or the loosening of cell sandwiched by two metal plates (see Figure 1), resulting in less accurate measured modulus values.

Figure 6a summarizes the average Young's moduli of the Si electrode throughout the successive delithiation from Li content x = 3.46 up to x = 1.54 in Li_xSi, with outliers (|SR| > 2.5) excluded. The whole measured moduli during the delithiation and the moduli with outliers (|SR| > 3 and 2) excluded are available in the Supporting Information (Figure S5). The measured modulus values of the Li_xSi throughout the subsequent delithiation are also consistent with the values obtained from theoretical calculations.[21,28] The changes in the contact radius R of the tip throughout the first delithiation

https://doi.org/10.1021/acs.jpclett.3c03012
J. Phys. Chem. Lett. 2024, 15, 490−498

(Figure 6b) were also recorded, and the values were within the normal contact radius range.[45]

In summary, we developed an *operando* bimodal atomic force microscopy (AFM) system to carry out nanomechanical mapping of an amorphous Si thin film electrode during successive lithiation/delithiation. Quantitative Young's modulus maps of the Si electrode were successfully acquired simultaneously with real-time cross-sectional surface topography images of the electrode. The average modulus of the Si electrode was in good agreement with those reported in the literature. This technique can be applied for a wide range of battery materials not only in an all-solid-state configuration but also in a liquid-type cell to clarify the mechanism of mechanical degradation initiated by phase transition and volume change in nanoscale accompanied by changes in mechanical property, which is crucial in the design of highly efficient and durable LIBs.

■ ASSOCIATED CONTENT

Supporting Information

The Supporting Information is available free of charge at https://pubs.acs.org/doi/10.1021/acs.jpclett.3c03012.

Experimental challenges (typical influences of ion milling on the cross-section, first lithiation capacity, nanomechanical map, and interfacial fragility of Si electrode) and recorded average Young's moduli of Si electrode during the first lithiation/delithiation (PDF)

■ AUTHOR INFORMATION

Corresponding Author

Takuya Masuda − *Graduate School of Chemical Sciences and Engineering, Hokkaido University, Sapporo, Hokkaido 060-0810, Japan; Research Center for Energy and Environmental Materials (GREEN), National Institute for Materials Science (NIMS), Tsukuba, Ibaraki 305-0044, Japan;* orcid.org/0000-0001-7462-2177; Email: MASUDA.Takuya@nims.go.jp

Authors

Ridwan P. Putra − *Graduate School of Chemical Sciences and Engineering, Hokkaido University, Sapporo, Hokkaido 060-0810, Japan; Research Center for Energy and Environmental Materials (GREEN), National Institute for Materials Science (NIMS), Tsukuba, Ibaraki 305-0044, Japan;* orcid.org/0000-0002-4941-4103

Kyosuke Matsushita − *Research Center for Energy and Environmental Materials (GREEN), National Institute for Materials Science (NIMS), Tsukuba, Ibaraki 305-0044, Japan*

Tsuyoshi Ohnishi − *Research Center for Energy and Environmental Materials (GREEN), National Institute for Materials Science (NIMS), Tsukuba, Ibaraki 305-0044, Japan;* orcid.org/0000-0002-2333-7752

Complete contact information is available at: https://pubs.acs.org/10.1021/acs.jpclett.3c03012

Notes

The authors declare no competing financial interest.

■ ACKNOWLEDGMENTS

The authors acknowledge the financial support provided by the Center of Innovation NEXT Program (COI-NEXT) of Japan Science and Technology Agency (JST; Grant Number JPMJPF2016) and the Materials Processing Science project "Materealize" of the Ministry of Education, Culture, Sports, Science and Technology of Japan (MEXT; Grant Number JPMXP0219207397). We also acknowledge the NIMS Battery Platform for their technical support.

■ REFERENCES

(1) Kim, T.; Song, W.; Son, D.-Y.; Ono, L. K.; Qi, Y. Lithium-ion batteries: outlook on present, future, and hybridized technologies. *Journal of Materials Chemistry A* **2019**, *7* (7), 2942−2964.

(2) Jun, D.-W.; Yoon, C. S.; Kim, U.-H.; Sun, Y.-K. High-Energy Density Core-Shell Structured $Li[Ni_{0.95}Co_{0.025}Mn_{0.025}]O_2$ Cathode for Lithium-Ion Batteries. *Chem. Mater.* **2017**, *29* (12), 5048−5052.

(3) Lu, L.; Han, X.; Li, J.; Hua, J.; Ouyang, M. A review on the key issues for lithium-ion battery management in electric vehicles. *J. Power Sources* **2013**, *226*, 272−288.

(4) Kalhoff, J.; Eshetu, G. G.; Bresser, D.; Passerini, S. Safer Electrolytes for Lithium-Ion Batteries: State of the Art and Perspectives. *ChemSusChem* **2015**, *8* (13), 2154−2175.

(5) Iwama, T.; Ohnishi, T.; Masuda, T. Operando Observation of Lithiation and Delithiation Reactions of a $LiCoO_2$-Li_3BO_3 Composite Electrode Formed on a $Li_{6.6}La_3Zr_{1.6}Ta_{0.4}O_{12}$ Solid Electrolyte Sheet by Laboratory-based Hard X-ray Photoelectron Spectroscopy. *Electrochemistry* **2023**, *91* (11), 117005.

(6) Sun, Y.-K. Promising All-Solid-State Batteries for Future Electric Vehicles. *ACS Energy Letters* **2020**, *5* (10), 3221−3223.

(7) Yue, L.; Ma, J.; Zhang, J.; Zhao, J.; Dong, S.; Liu, Z.; Cui, G.; Chen, L. All solid-state polymer electrolytes for high-performance lithium ion batteries. *Energy Storage Materials* **2016**, *5*, 139−164.

(8) Domi, Y.; Usui, H.; Shimizu, M.; Kakimoto, Y.; Sakaguchi, H. Effect of Phosphorus-Doping on Electrochemical Performance of Silicon Negative Electrodes in Lithium-Ion Batteries. *ACS Appl. Mater. Interfaces* **2016**, *8* (11), 7125−7132.

(9) Domi, Y.; Usui, H.; Sugimoto, K.; Sakaguchi, H. Effect of Silicon Crystallite Size on Its Electrochemical Performance for Lithium-Ion Batteries. *Energy Technology* **2019**, *7* (5), 1800946.

(10) Domi, Y.; Usui, H.; Yamaguchi, K.; Yodoya, S.; Sakaguchi, H. Silicon-Based Anodes with Long Cycle Life for Lithium-Ion Batteries Achieved by Significant Suppression of Their Volume Expansion in Ionic-Liquid Electrolyte. *ACS Appl. Mater. Interfaces* **2019**, *11* (3), 2950−2960.

(11) Nguyen, C. C.; Lucht, B. L. Comparative Study of Fluoroethylene Carbonate and Vinylene Carbonate for Silicon Anodes in Lithium Ion Batteries. *J. Electrochem. Soc.* **2014**, *161* (12), A1933.

(12) Ohta, N.; Kimura, S.; Sakabe, J.; Mitsuishi, K.; Ohnishi, T.; Takada, K. Anode Properties of Si Nanoparticles in All-Solid-State Li Batteries. *ACS Applied Energy Materials* **2019**, *2* (10), 7005−7008.

(13) Tan, D. H. S.; Chen, Y.-T.; Yang, H.; Bao, W.; Sreenarayanan, B.; Doux, J.-M.; Li, W.; Lu, B.; Ham, S.-Y.; Sayahpour, B.; Scharf, J.; Wu, E. A.; Deysher, G.; Han, H. E.; Hah, H. J.; Jeong, H.; Lee, J. B.; Chen, Z.; Meng, Y. S. Carbon-free high-loading silicon anodes enabled by sulfide solid electrolytes. *Science* **2021**, *373* (6562), 1494−1499.

(14) Ferraresi, G.; El Kazzi, M.; Czornomaz, L.; Tsai, C.-L.; Uhlenbruck, S.; Villevieille, C. Electrochemical Performance of All-Solid-State Li-Ion Batteries Based on Garnet Electrolyte Using Silicon as a Model Electrode. *ACS Energy Letters* **2018**, *3* (4), 1006−1012.

(15) Kim, J.; Kim, C.; Jang, I.; Park, J.; Kim, J.; Paik, U.; Song, T. Si nanoparticles embedded in carbon nanofiber sheathed with Li_6PS_5Cl as an anode material for all-solid-state batteries. *J. Power Sources* **2021**, *510*, 230425.

(16) Obrovac, M. N.; Christensen, L. Structural Changes in Silicon Anodes during Lithium Insertion/Extraction. *Electrochem. Solid-State Lett.* **2004**, *7* (5), A93.

(17) Wang, H.; Xie, J.; Zhang, S.; Cao, G.; Zhao, X. Scalable preparation of silicon@graphite/carbon microspheres as high-

performance lithium-ion battery anode materials. *RSC Adv.* **2016**, *6* (74), 69882−69888.
(18) Yan, N.; Wang, F.; Zhong, H.; Li, Y.; Wang, Y.; Hu, L.; Chen, Q. Hollow Porous SiO_2 Nanocubes Towards High-performance Anodes for Lithium-ion Batteries. *Sci. Rep.* **2013**, *3* (1), 1568.
(19) Nakano, H.; Oh-ishi, K.; Matsubara, M. Tailoring the Void Space of a Silicon Anode for High-Capacity and Low-Expansion Lithium Storage. *Energy Technology* **2022**, *10* (11), 2200236.
(20) Demirkan, M. T.; Trahey, L.; Karabacak, T. Cycling performance of density modulated multilayer silicon thin film anodes in Li-ion batteries. *J. Power Sources* **2015**, *273*, 52−61.
(21) Kim, H.; Chou, C.-Y.; Ekerdt, J. G.; Hwang, G. S. Structure and Properties of Li-Si Alloys: A First-Principles Study. *J. Phys. Chem. C* **2011**, *115* (5), 2514−2521.
(22) Chen, C.-Y.; Sano, T.; Tsuda, T.; Ui, K.; Oshima, Y.; Yamagata, M.; Ishikawa, M.; Haruta, M.; Doi, T.; Inaba, M.; Kuwabata, S. In situ Scanning Electron Microscopy of Silicon Anode Reactions in Lithium-Ion Batteries during Charge/Discharge Processes. *Sci. Rep.* **2016**, *6* (1), 36153.
(23) Inaba, M.; Haruta, M.; Saito, M.; Doi, T. Silicon Nano-flake Powder as an Anode for The Next Generation Lithium-ion Batteries: Current Status and Challenges. *Electrochemistry* **2017**, *85* (10), 623−629.
(24) Cervera, R. B.; Suzuki, N.; Ohnishi, T.; Osada, M.; Mitsuishi, K.; Kambara, T.; Takada, K. High performance silicon-based anodes in solid-state lithium batteries. *Energy Environ. Sci.* **2014**, *7* (2), 662−666.
(25) Sakabe, J.; Ohta, N.; Ohnishi, T.; Mitsuishi, K.; Takada, K. Porous amorphous silicon film anodes for high-capacity and stable all-solid-state lithium batteries. *Communications Chemistry* **2018**, *1* (1), 24.
(26) Endo, R.; Ohnishi, T.; Takada, K.; Masuda, T. Electrochemical Lithiation and Delithiation in Amorphous Si Thin Film Electrodes Studied by Operando X-ray Photoelectron Spectroscopy. *J. Phys. Chem. Lett.* **2022**, *13* (31), 7363−7370.
(27) Gao, H.; Xiao, L.; Plümel, I.; Xu, G.-L.; Ren, Y.; Zuo, X.; Liu, Y.; Schulz, C.; Wiggers, H.; Amine, K.; Chen, Z. Parasitic Reactions in Nanosized Silicon Anodes for Lithium-Ion Batteries. *Nano Lett.* **2017**, *17* (3), 1512−1519.
(28) Shenoy, V. B.; Johari, P.; Qi, Y. Elastic softening of amorphous and crystalline Li-Si Phases with increasing Li concentration: A first-principles study. *J. Power Sources* **2010**, *195* (19), 6825−6830.
(29) Komori, C.; Ishikawa, S.; Nunoshita, K.; So, M.; Kimura, N.; Inoue, G.; Tsuge, Y. Stress Prediction of the Particle Structure of All-Solid-State Batteries by Numerical Simulation and Machine Learning. *Frontiers in Chemical Engineering* **2022**, *4*, 836282.
(30) Zeng, Z.; Liu, N.; Zeng, Q.; Ding, Y.; Qu, S.; Cui, Y.; Mao, W. L. Elastic moduli of polycrystalline $Li_{15}Si_4$ produced in lithium ion batteries. *J. Power Sources* **2013**, *242*, 732−735.
(31) Iwasa, H.; Ikemoto, S.; Ohashi, F.; S. Jha, H.; Kume, T. X-Ray Diffraction Investigation of Lithium Silicides under High Pressure. *JJAP Conference Proceedings* **2020**, *8*, 011302−011302.
(32) Hertzberg, B.; Benson, J.; Yushin, G. Ex-situ depth-sensing indentation measurements of electrochemically produced Si-Li alloy films. *Electrochem. Commun.* **2011**, *13* (8), 818−821.
(33) Ono, Y.; Kumaki, J. In Situ Real-Time Observation of Polymer Folded-Chain Crystallization by Atomic Force Microscopy at the Molecular Level. *Macromolecules* **2018**, *51* (19), 7629−7636.
(34) Wang, D.; Russell, T. P. Advances in Atomic Force Microscopy for Probing Polymer Structure and Properties. *Macromolecules* **2018**, *51* (1), 3−24.
(35) Rajendran, A.; Endo, M.; Sugiyama, H. State-of-the-Art High-Speed Atomic Force Microscopy for Investigation of Single-Molecular Dynamics of Proteins. *Chem. Rev.* **2014**, *114* (2), 1493−1520.
(36) Masuda, T.; Sonsudin, F.; Singh, P. R.; Naohara, H.; Uosaki, K. Potential-Dependent Adsorption and Desorption of Perfluorosulfonated Ionomer on a Platinum Electrode Surface Probed by Electrochemical Quartz Crystal Microbalance and Atomic Force Microscopy. *J. Phys. Chem. C* **2013**, *117* (30), 15704−15709.
(37) Kasuya, M.; Sogawa, T.; Masuda, T.; Kamijo, T.; Uosaki, K.; Kurihara, K. Anion Adsorption on Gold Electrodes Studied by Electrochemical Surface Forces Measurement. *J. Phys. Chem. C* **2016**, *120* (29), 15986−15992.
(38) Devivaraprasad, R.; Masuda, T. Solvent-Dependent Adsorption of Perfluorosulfonated Ionomers on a Pt(111) Surface Using Atomic Force Microscopy. *Langmuir* **2020**, *36* (46), 13793−13798.
(39) Jiang, H.; Peng, H.; Guo, H.; Zeng, Y.; Li, L.; Zhang, Y.; Chen, Y.; Chen, X.; Zhang, J.; Chu, R. Interfacial Mechanical Strength Enhancement for High-Performance ZnS Thin-Film Anodes. *ACS Appl. Mater. Interfaces* **2020**, *12* (46), 51344−51356.
(40) Kempaiah, R.; Vasudevamurthy, G.; Subramanian, A. Scanning probe microscopy based characterization of battery materials, interfaces, and processes. *Nano Energy* **2019**, *65*, 103925.
(41) Legerstee, W. J.; Boekel, M.; Boonstra, S.; Kelder, E. M. Scanning Probe Microscopy Facility for Operando Study of Redox Processes on Lithium ion Battery Electrodes. *Frontiers in Chemistry* **2021**, *9*, 505876.
(42) Terreblanche, J. S.; Thompson, D. L.; Aldous, I. M.; Hartley, J.; Abbott, A. P.; Ryder, K. S. Experimental Visualization of Commercial Lithium Ion Battery Cathodes: Distinguishing Between the Microstructure Components Using Atomic Force Microscopy. *J. Phys. Chem. C* **2020**, *124* (27), 14622−14631.
(43) Zhang, Z.; Said, S.; Smith, K.; Jervis, R.; Howard, C. A.; Shearing, P. R.; Brett, D. J. L.; Miller, T. S. Characterizing Batteries by In Situ Electrochemical Atomic Force Microscopy: A Critical Review. *Adv. Energy Mater.* **2021**, *11* (38), 2101518.
(44) Sakai, H.; Taniguchi, Y.; Uosaki, K.; Masuda, T. Quantitative cross-sectional mapping of nanomechanical properties of composite films for lithium ion batteries using bimodal mode atomic force microscopy. *J. Power Sources* **2019**, *413*, 29−33.
(45) Kocun, M.; Labuda, A.; Meinhold, W.; Revenko, I.; Proksch, R. Fast, High Resolution, and Wide Modulus Range Nanomechanical Mapping with Bimodal Tapping Mode. *ACS Nano* **2017**, *11* (10), 10097−10105.
(46) Gisbert, V. G.; Benaglia, S.; Uhlig, M. R.; Proksch, R.; Garcia, R. High-Speed Nanomechanical Mapping of the Early Stages of Collagen Growth by Bimodal Force Microscopy. *ACS Nano* **2021**, *15* (1), 1850−1857.
(47) Yang, P.; Bi, Z.; Shang, Y.; Chen, K.; Liang, Y.; Li, X.; Shang, G. Bimodal AFM-Based Nanocharacterization of Cycling-Induced Topographic and Mechanical Evolutions of $LiMn_2O_4$ Cathode Films. *Langmuir* **2021**, *37* (21), 6406−6413.
(48) Hikima, K.; Hinuma, Y.; Shimizu, K.; Suzuki, K.; Taminato, S.; Hirayama, M.; Masuda, T.; Tamura, K.; Kanno, R. Reactions of the Li_2MnO_3 Cathode in an All-Solid-State Thin-Film Battery during Cycling. *ACS Appl. Mater. Interfaces* **2021**, *13* (6), 7650−7663.
(49) Shiraki, S.; Shirasawa, T.; Suzuki, T.; Kawasoko, H.; Shimizu, R.; Hitosugi, T. Atomically Well-Ordered Structure at Solid Electrolyte and Electrode Interface Reduces the Interfacial Resistance. *ACS Appl. Mater. Interfaces* **2018**, *10* (48), 41732−41737.
(50) Composites as Biomaterials. In *Biomaterials*; Park, J. B., Lakes, R. S., Eds.; Springer New York: New York, NY, 2007; pp 207−224.
(51) Endo, R.; Ohnishi, T.; Takada, K.; Masuda, T. In Situ Observation of Lithiation and Delithiation Reactions of a Silicon Thin Film Electrode for All-Solid-State Lithium-Ion Batteries by X-ray Photoelectron Spectroscopy. *J. Phys. Chem. Lett.* **2020**, *11* (16), 6649−6654.
(52) Li, W.; Yang, R.; Wang, X.; Wang, T.; Zheng, J.; Li, X. Intercalated Si/C films as the anode for Li-ion batteries with near theoretical stable capacity prepared by dual plasma deposition. *J. Power Sources* **2013**, *221*, 242−246.
(53) Loveridge, M. J.; Lain, M. J.; Johnson, I. D.; Roberts, A.; Beattie, S. D.; Dashwood, R.; Darr, J. A.; Bhagat, R. Towards High Capacity Li-ion Batteries Based on Silicon-Graphene Composite Anodes and Sub-micron V-doped $LiFePO_4$ Cathodes. *Sci. Rep.* **2016**, *6* (1), 37787.
(54) Ogata, K.; Salager, E.; Kerr, C. J.; Fraser, A. E.; Ducati, C.; Morris, A. J.; Hofmann, S.; Grey, C. P. Revealing lithium-silicide

phase transformations in nano-structured silicon-based lithium ion batteries via in situ NMR spectroscopy. *Nat. Commun.* **2014**, *5* (1), 3217.
(55) Hatchard, T. D.; Dahn, J. R. In Situ XRD and Electrochemical Study of the Reaction of Lithium with Amorphous Silicon. *J. Electrochem. Soc.* **2004**, *151* (6), A838.
(56) Labuda, A.; Kocuń, M.; Meinhold, W.; Walters, D.; Proksch, R. Generalized Hertz model for bimodal nanomechanical mapping. *Beilstein J. Nanotechnol* **2016**, *7*, 970−82.
(57) Hu, S.; Xu, P.; de Vasconcelos, L. S.; Stanciu, L.; Ni, H.; Zhao, K. Elastic Modulus, Hardness, and Fracture Toughness of $Li_{6.4}La_3Zr_{1.4}Ta_{0.6}O_{12}$ Solid Electrolyte. *Chin. Phys. Lett.* **2021**, *38* (9), 098401.
(58) Wang, X.; Singh, S. S.; Ma, T.; Lv, C.; Chawla, N.; Jiang, H. Quantifying Electrochemical Reactions and Properties of Amorphous Silicon in a Conventional Lithium-Ion Battery Configuration. *Chem. Mater.* **2017**, *29* (14), 5831−5840.
(59) Xu, H.; Yu, Y.; Wang, Z.; Shao, G. First Principle Material Genome Approach for All Solid-State Batteries. *Energy Environ. Mater.* **2019**, *2* (4), 234−250.
(60) Schneider, C. A.; Rasband, W. S.; Eliceiri, K. W. NIH Image to ImageJ: 25 years of image analysis. *Nat. Methods* **2012**, *9* (7), 671−675.
(61) Oliver, W. C.; Pharr, G. M. An improved technique for determining hardness and elastic modulus using load and displacement sensing indentation experiments. *J. Mater. Res.* **1992**, *7* (6), 1564−1583.
(62) Wolfenstine, J.; Allen, J. L.; Sakamoto, J.; Siegel, D. J.; Choe, H. Mechanical behavior of Li-ion-conducting crystalline oxide-based solid electrolytes: a brief review. *Ionics* **2018**, *24* (5), 1271−1276.
(63) Huang, S.; Zhu, T. Atomistic mechanisms of lithium insertion in amorphous silicon. *J. Power Sources* **2011**, *196* (7), 3664−3668.
(64) Jerliu, B.; Hüger, E.; Dörrer, L.; Seidlhofer, B. K.; Steitz, R.; Oberst, V.; Geckle, U.; Bruns, M.; Schmidt, H. Volume Expansion during Lithiation of Amorphous Silicon Thin Film Electrodes Studied by In-Operando Neutron Reflectometry. *J. Phys. Chem. C* **2014**, *118* (18), 9395−9399.
(65) Arimie, C. O.; Biu, E. O.; Ijomah, M. A. Outlier Detection and Effects on Modeling. *Open Access Library Journal* **2020**, *7* (9), e6619.
(66) Detecting Influential Observations and Outliers. *Regression Diagnostics*; Wiley, 1980; pp 6−84, .
(67) Bucci, G.; Nadimpalli, S. P. V.; Sethuraman, V. A.; Bower, A. F.; Guduru, P. R. Measurement and modeling of the mechanical and electrochemical response of amorphous Si thin film electrodes during cyclic lithiation. *J. Mech. Phys. Solids* **2014**, *62*, 276−294.
(68) Gaire, C.; Ye, D. X.; Tang, F.; Picu, R. C.; Wang, G. C.; Lu, T. M. Mechanical Testing of Isolated Amorphous Silicon Slanted Nanorods. *J. Nanosci. Nanotechnol.* **2005**, *5* (11), 1893−1897.
(69) Sitinamaluwa, H.; Nerkar, J.; Wang, M.; Zhang, S.; Yan, C. Deformation and failure mechanisms of electrochemically lithiated silicon thin films. *RSC Adv.* **2017**, *7* (22), 13487−13497.
(70) Kubota, Y.; Escaño, M. C. S.; Nakanishi, H.; Kasai, H. Crystal and electronic structure of $Li_{15}Si_4$. *J. Appl. Phys.* **2007**, *102* (5), 053704.

https://doi.org/10.1021/acs.jpclett.3c03012
J. Phys. Chem. Lett. 2024, 15, 490−498